Metastable β-Phase Ti–Nb Alloys Fabricated by Powder Metallurgy: Effect of Nb on Superelasticity and Deformation Behavior

D. KALITA, K. MULEWSKA, I. JÓŹWIK, A. ZABOROWSKA, M. GAWĘDA, W. CHROMIŃSKI, K. BOCHENEK, and Ł. ROGAL

This study investigates the effect of Nb concentration on the mechanical properties, superelasticity, as well as deformation behavior of metastable β-phase Ti–Nb alloys produced via powder metallurgy. The alloys were fabricated through mechanical alloying, followed by consolidation using hot pressing. The resulting microstructure comprises fine β-phase grains with TiC carbide precipitates at the grain boundaries. The study reveals non-linear variations in the values of yield strength for the manufactured materials, which were attributed to the occurrence of various deformation mechanisms activated during the loading. It was found that the mechanisms change with the increasing concentration of Nb in the manner: stress-induced martensitic transformation, twinning, slip. However, all these mechanisms were activated at a reduced concentration of Nb compared to the materials obtained by casting technology previously reported in the literature. This is most probably associated with the elevated oxygen content, which affects the stability of the parent β-phase. The study revealed that superelasticity in Ti–Nb-based alloys prepared using powder metallurgy may be achieved by reducing the content of β-stabilizing elements compared to alloys obtained by conventional technologies. In this study, the Ti–14Nb (at. pct) alloy exhibited the best superelasticity, whereas conventionally fabricated Ti–Nb alloys displayed superelasticity at an Nb concentration of approximately 26 at. pct. The developed material exhibited a non-conventional, one-stage yielding behavior, resulting in a superelastic response at significantly higher stresses compared to conventionally fabricated Ti–Nb alloys.

I. INTRODUCTION

THE β-phase Ti alloys are currently attracting significant attention as a highly promising group of metallic materials for biomedical applications.[1] It is attributed to their superior mechanical properties, reduced elastic modulus, excellent biocompatibility, and corrosion resistance.[2–4] Concerning the materials utilized for the bone implants, they must satisfy certain requirements, *i.e.*, the absence of toxic elements and appropriate mechanical properties corresponding to these observed for the bones.[5] Unfortunately, they are incompletely fulfilled for the Ti alloys currently used in implantology, for instance Ti–6Al–4V, because of the presence of Al that may contribute to the development of Alzheimer's disease.[2,5] To overcome this problem, a novel class of biocompatible β-Ti alloys, which contain non-toxic alloying elements, such as Nb, Zr, or Ta, was developed. Recent studies show that except aforementioned advantages, the β-Ti alloys exhibit also shape memory and superelastic effects.[6–8] In the context of biomedical applications, the latter phenomenon appears to be the most significant, as the mechanical behavior of superelastic materials is comparable to that observed in bones.[9] The superelasticity is related to the occurrence of the reversible stress-induced martensitic transformation (SIMT). In β-Ti alloys, the transformation occurs between the body-centered cubic (BCC) β-Ti austenite and the orthorhombic α''-martensite.[10] Up to now, the

D. KALITA, K. MULEWSKA, I. JÓŹWIK, A. ZABOROWSKA, and M. GAWĘDA are with the NOMATEN Centre of Excellence, National Centre for Nuclear Research, A. Sołtana 7, 05-400 Otwock-Świerk, Poland. Contact e-mail: Damian.Kalita@ncbj.gov.pl W. CHROMIŃSKI is with the NOMATEN Centre of Excellence, National Centre for Nuclear Research and also with the Faculty of Materials Science and Engineering, Warsaw University of Technology, Wołoska 141 St., 02-507 Warsaw, Poland. K. BOCHENEK is with the Institute of Fundamental Technological Research, Polish Academy of Sciences, Pawińskiego 5B, 02-106, Warsaw, Poland. Ł. ROGAL is with the Institute of Metallurgy and Materials Science, Polish Academy of Sciences, Reymonta 25, 30–059 Krakow, Poland.

superelastic properties were found in numerous binary and ternary β-Ti alloys, *e.g.*, Ti–26Nb,[11] Ti–18Nb–3Mo,[6] or Ti–6Mo–3Ga.[12] In the Ti–Nb system, the phenomenon was registered for alloys containing 26-27 at. pct of Nb.[10,11] Such materials typically exhibit recoverable strains ranging between 1 and 2.5 pct[11,13,14] in a solution-treated (ST) state. These values may be slightly enhanced by rising the critical stress required for slip. For instance, the presence of nanoscale precipitates of ω-phase in the aged alloys can boost the recoverable strain to around 4 pct.[11]

Current advancements in manufacturing of Ti alloys are primarily centered around the utilization of powder metallurgy (PM) and additive manufacturing (AM).[15,16] These advanced technologies enable the preparation of parts with unique microstructures and enhanced mechanical properties, which are frequently challenging or unattainable to obtain by the conventional approaches. Despite this, there is a lack of comprehensive analysis in the literature concerning the mechanical and superelastic properties of β-phase titanium alloys fabricated using the PM technique. The available data indicate that they typically exhibit increased strength, reduced ductility and, diminished superelasticity compared to their conventional counterparts.[17–19] For example, Chen *et al.*[17] reported that a yield strength (YS) for pressureless sintered Ti–26Nb reached about 600 MPa, whereas these values did not exceed 400 MPa for the cast alloys.[13,14] The values varied from $\approx$ 800 to $\approx$ 1300 MPa were registered for the series of sintered Ti–(8–18)Nb.[18] Even higher value close to 1.5 GPa, accompanied by poor ductility, were reported for the pressureless sintered Ti–11Nb.[19] On the other hand, the data regarding the superelastic characteristics of such materials are even more limited. Preliminary investigations concerning this issue revealed the absence of superelasticity in the sintered materials, despite it being previously registered for conventionally fabricated alloys with the same compositions.[20–22] More recently, Lai *et al.*[18] found that the superelasticity in the sintered Ti–Nb alloys may be obtained by the reduction of the concentration of Nb to approximately 13 at. pct. The alloy possesses a high recoverable strain of about 5 pct. However, the value was mainly associated with the combination of the high YS (of about 1 GPa) and elevated elasticity of the alloy. Similar behavior was observed by Yuan *et al.*[19] in sintered Ti–11Nb alloy, which exhibits 5.4 pct of recoverable strain and an extremely high strength of about 1500 MPa. Unfortunately, the data concerning the evolution of both mechanical as well as superelastic properties with respect to the content of the β-stabilizing elements in PM-fabricated β-titanium alloys are very limited. The description of this effect allows for a deeper understanding of the properties of this novel group of materials and for the development of new compositions of alloys dedicated for fabrication using the PM technology, with enhanced performance.

Therefore, the presented work aimed to fabricate a series of binary Ti–Nb alloys using the PM route and study the influence of Nb concentration on the mechanical and superelastic properties of these materials. To gain a more detailed understanding of their performance, the materials underwent a thorough analysis of the microstructural effects occurring during their deformation.

II. EXPERIMENTAL

A. *Materials Fabrication*

The investigated Ti–14Nb, Ti–20Nb and Ti–26Nb (in at. pct) alloys were prepared using mechanical alloying (MA) and hot pressing (HP) techniques. The powders of Ti ($< 105\ \mu m$, 99.9 + pct) and Nb ($< 44\ \mu m$, 99.8 + pct) supplied by Alfa Aesar were applied. The MA process was conducted using a Fritsch Pulverisette 7 planetary ball mill. The following synthesis conditions were applied: rotation speed 150 rpm, time 30 hours, ball-to-powder ratio 10:1. The vessel and balls (5 mm), made of cemented tungsten carbide, were used. In order to prevent contamination of the powders, all powder-related procedures were performed within a glovebox, ensuring an argon atmosphere with O_2 and H_2O levels maintained below 1 ppm. The sintering was conducted using a Thermal Technology HP-20-4650 hot pressing system. The following sintering conditions were applied: temperature 1400 °C, time 30 minutes, pressure 50 MPa, heating rate 10 °C/min. The process was conducted under a vacuum (10^{-3} Pa). Cylindrical samples with a diameter of 24 mm and a height of around 10 mm were obtained. In the next step, the materials were solution-treated at 1250 °C for 24 hours to enhance their chemical homogeneity. The samples were encapsulated in quartz tubes under a vacuum to prevent oxidation during the annealing.

B. *Materials Characterization*

The phase composition of the fabricated alloys was studied by X-ray diffraction (XRD) method with the application of a Philips PW1740 diffractometer and Co Kα radiation. Microstructural investigations were performed with the application of a ThermoFisher Scientific Helios 5 UX dual beam scanning electron microscope (SEM). The microscope was equipped with the EDAX Octane Elite Plus energy-dispersive X-ray spectroscopy (EDS) system and the EDAX velocity electron backscatter diffraction (EBSD) camera. The transmission electron microscopy (TEM) observations were carried out using a JEOL JEM 1200EX II (120 kV) and JEOL JEM F-200 (200 kV) microscopes. The thin foils for the TEM investigations were prepared by a focused ion beam (FIB) lift-out technique. The oxygen concentration in the fabricated alloys was measured by inert gas fusion (IGF) method by a Leco ON836. For each of the compositions, three samples with a weight of about 0.5 g were used. Carbon, nitrogen and hydrogen concentration were measured by laser-induced breakdown spectroscopy (LIBS) method using the J200 Tandem system (Applied Spectra Inc., Fremont, CA) controlled by the Axiom software. Samples were analyzed with a 213 nm Nd:YAG laser. The measurements

were conducted in an atmosphere of noble gas (argon) with a flow of 2 L/min. Additionally, the sample chamber was purged prior to collecting spectra for 200 seconds. The laser's energy was set at 50 pct. Spectra were obtained from 8 points within a $250 \times 500 \ \mu m$ frame, with 64 laser shots per point and 20 Hz repetition rate, precede by 25 warmup shots. Prior to the measurement, the surface of the samples was ablated to remove surface layer and potential environmental contaminations. For the calibration curves, certified referential materials of titanium alloys (MBH Analytical LTD, High Barnet, UK) were used, specifically IARM-TiG4-18, IARM-Ti64-18 (6-4), and IARM-Ti64ELI-18 (6Ai-4V ELI).

Mechanical properties of the materials were studied in compression and tension. The compression tests were performed with the application of Shimadzu Autograph AG-X machine. The tests were carried out with a strain rate of 10^{-3} 1/s at room temperature (RT). The tested samples with the cylindrical shape (diameter 4 mm, height 6 mm) were fabricated with the application of a wire electrical discharge machining (WEDM). Tensile tests were performed at RT on a ZwickRoell Z020 AllroundLine machine equipped with a 10 kN load cell. In the tests, strain was measured directly by non-contact laser measurement technique using a ZwickRoell laserXtens system. All tensile samples were machined from the bulk using WEDM method. In order to remove the material layer affected by cutting, before final testing, samples where mechanically grinded with SiC abrasive paper (1200 grade). The miniature geometry of the samples includes a gauge length of 4 mm and a thickness of 0.6 mm. Tests were performed with closed-loop strain control and a strain rate of 0.00025 1/s. For each of the materials, three samples were tested in both compression and tension.

The superelasticity of the alloys were studied by cyclic compression tests. The experiments were conducted on a single sample, gradually increasing the strain by 0.5 pct per cycle, starting from 1 pct and progressing up to 5 pct of the total strain. After each cycle, the stress was removed. The recoverable strain was defined as a difference between the maximum strain and permanent strain after the last cycle.[23] Three samples were measured for each alloy. The in situ deformation studies were performed with the application of a home-made tensile device allowing for the observation of the microstructure of deformed material by visible light microscope. The experiments were conducted on dog bone-shaped samples, featuring the following dimensions: gauge length of 8 mm, width of 2 mm, and a thickness of approximately 300 μm. The microstructural effects resulting from the deformation were investigated after deformation up to 2 pct and in the unloaded state. Nanoindentation tests were performed at RT using a Micro Materials Ltd NanoTest Vantage system. A spherical indenter with tip radius of 5 μm was used. To study the superelasticity of the investigated materials the depth recovery ratio η_{h} (Eq. 1) and work recovery ratio η_{w} (Eq. 2) were extracted from nanoindentation load–depth (F–h) curves.[24,25] The η_{h} may be described as:

$$\eta_{h} = \frac{h_{m} - h_{p}}{h_{m}}, \qquad [1]$$

where h_{m} is maximum penetration depth and h_{p} is permanent indentation depth after the unloading. On the other hand, the η_{w} (Eq. 2) may be defined as the ratio of recoverable work W_{rc} to the total work W_{t}:

$$\eta_{w} = \frac{W_{rc}}{W_{t}} = \frac{\int_{h_{p}}^{h_{m}} F dh}{\int_{0}^{h_{m}} F dh}. \qquad [2]$$

Indentations were performed in a single force mode using various loads: 5, 10, 15, 20, 25, 30 mN (Ti–14Nb) and 5, 10, 15, 20 mN (Ti–20Nb and Ti–26Nb).

III. RESULTS

A. Phase Composition and Microstructure

Figure 1(a) shows the XRD patterns registered for the investigated Ti–xNb alloys. All alloys contain mainly the BCC β-Ti phase, but the peaks corresponding to the orthorhombic α''-martensite may be also distinguished for Ti–14Nb. This indicates that the M_{s} (martensite start) temperature for this alloy is slightly above RT. Figure 1(b) presents the typical microstructure of the investigated alloys. It comprised relatively fine grains of β-Ti with micrometric precipitates (marked with yellow frame in Figure 1(b)) located mainly at grain boundaries (visible as dark). Their total fraction was independent of the Nb concentration and reached about 1 vol pct in all alloys (based on the stereological measurements using planimetric method). The performed EDS mapping indicates that the precipitates were enriched in Ti and C, but depleted in Nb. To investigate their nature in more detail the TEM technique was used. The selected area electron diffraction (SAED) pattern taken from the particle corresponds to the cubic structure of $Fm3m$-TiC$_{x}$ carbide—Figure 1(c). The occurrence of the superlattice maxima resulting from the vacancy related ordering of TiC$_{x}$ carbide which typically exists over a wide stoichiometric ratio ($0.5 \leq x \leq 1$), as described in more details in References 26 and 27. Because of that, the occurrence of $Fd3m$-Ti$_{2}$C was suggested by some studies, e.g., References 28 and 29. The presence of the TiC$_{x}$ was previously reported in variety of titanium alloys prepared using powder metallurgy route, e.g., Ti–15Mo[28] or Ti–xNb.[30] The orientation map presented in Figure 1(d) shows that the materials did not exhibit a visible crystallographic texture, which was confirmed by calculated inverse pole figure (IPF) (presented as inset in Figure 1(d)). The performed grain size analysis (presented in Table I) indicates that the average size of the grains slightly decrease with the increasing Nb concentration, ranging from $47 \pm 28 \ \mu m$ for Ti–14Nb to $21 \pm 13 \ \mu m$ for Ti–26Nb. It is noteworthy that the developed sintering procedure led to the production of nearly fully dense alloys, with a porosity level below 0.1 vol pct. The chemical composition of the alloys quantified by an
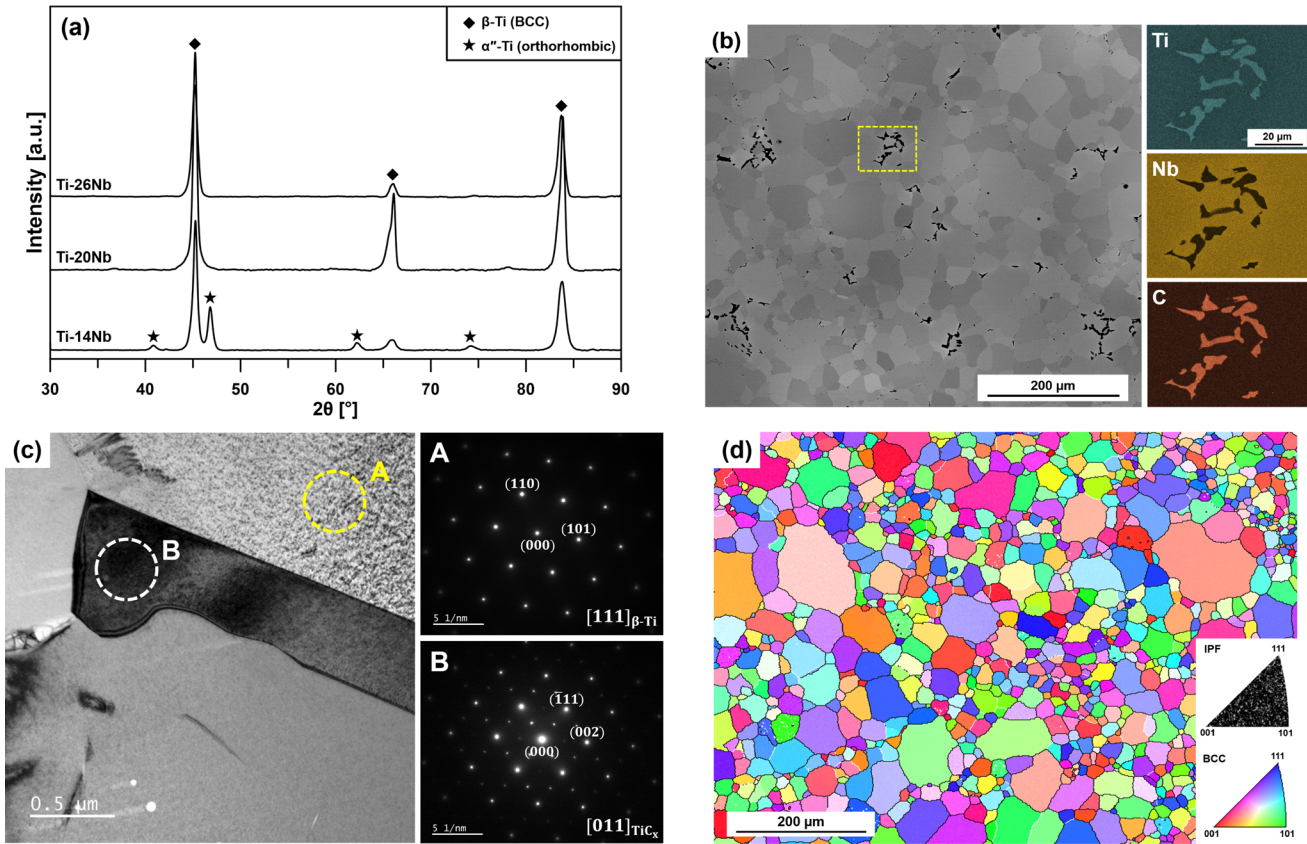
Fig. 1—XRD patterns of the investigated alloys (*a*), microstructure (BSE contrast) of the Ti–20Nb alloy, with the corresponding EDS elemental maps (*b*), BF/TEM micrograph and corresponding SAED patterns from the area of matrix (A) and precipitate from the grain boundary (B) (*c*) and EBSD orientation map with the corresponding IPF as an inset (*d*).

Table I. Average Grain Size and Concentration of Nb, O, C, N and H in the Investigated Alloys

Alloy (At. Pct]	Ti–14Nb	Ti–20Nb	Ti–26Nb
Average Grain Size (μm)	47 ± 28	26 ± 16	21 ± 13
Nb Concentration (EDS) (At. Pct)	14.5 ± 0.5	20.3 ± 0.4	26.4 ± 0.3
O Concentration (IGF) (At. Pct)	0.59 ± 0.04	0.52 ± 0.02	0.57 ± 0.05
C Concentration (LIBS) (At. Pct)	0.16 ± 0.02	0.10 ± 0.01	0.08 ± 0.01
N Concentration (LIBS) (At. Pct)	0.02 ± 0.01	0.01 ± 0.01	0.01 ± 0.01
H Concentration (LIBS) (At. Pct)	0.08 ± 0.01	0.07 ± 0.01	0.09 ± 0.01

EDS presented in Table I corresponds to the intended values and the changes do not exceed 0.5 at. pct. Using the IGF method we found that the oxygen concentration in the investigated materials reaches 0.5 to 0.6 at. pct.

In order to study the microstructure of the fabricated materials in more detail, the TEM technique was used. Figure 2(a) displays the BF/TEM microstructure of the Ti–14Nb alloy. The corresponding diffraction pattern (Figure 2(b)) registered along the $[001]_\beta$ zone axis, revealed additional refractions that could be indexed as orthorhombic α''-martensite. This finding aligns well with the XRD results (Figure 1(a)), indicating the presence of martensite in Ti–14Nb alloy. The observed orientation relationship between the α''-Ti and parent β-Ti phase was: $[011]_{\beta-Ti}//[020]_{\alpha''-Ti}$. As shown in the

dark-field (DF) image (Figure 2(c)), the α''-martensite appeared in the form of nanometric needles surrounded by the β-Ti matrix. It is essential to note that the α''-martensite was not observed in the other samples, *i.e.*, Ti–20Nb and Ti–26Nb.

Further investigations of the parent β-phase revealed the presence of precipitates of a secondary phase, as shown in Figure 3. The SAED patterns acquired along the $[110]_\beta$ zone axis not only contain the primary β-Ti reflections but also show diffuse scattering at 1/3 and 2/3 $\{\bar{1}12\}_\beta$, corresponding to the hexagonal ω-phase (*P6/mmm*). In general, two types of ω-phase can be distinguished based on their formation mechanisms: (I) athermal ω-phase (ω_{ath}), which arises during quenching through the displacive mechanism, and (II) isothermal ω-phase (ω_{iso}), which forms during intermediate aging
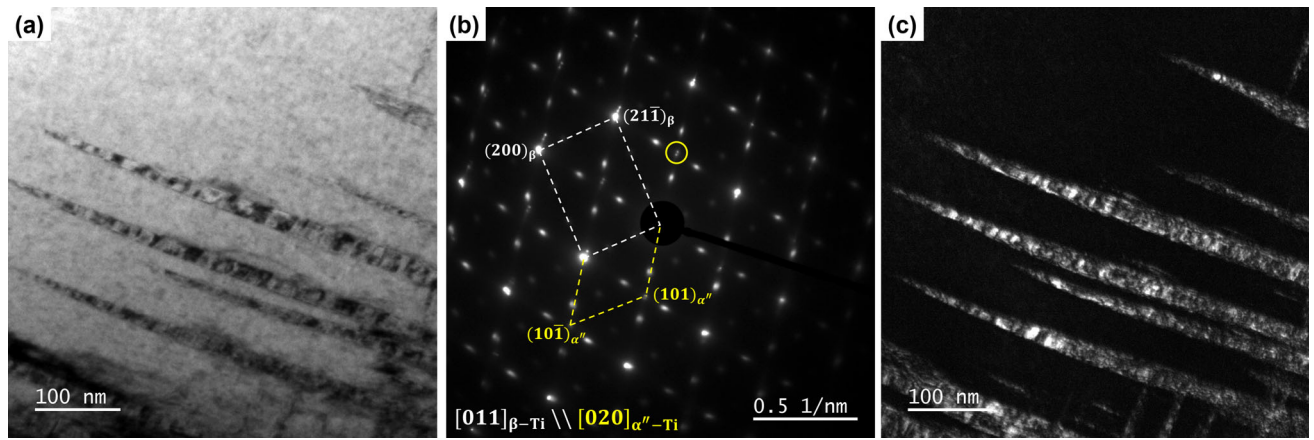
Fig. 2—BF/TEM micrograph of the Ti–14Nb sample (*a*) with the corresponding SAED pattern (*b*) and the DF/TEM image (*c*) selecting the α″-martensite reflection, highlighted in the SAED with the yellow circle (Color figure online).
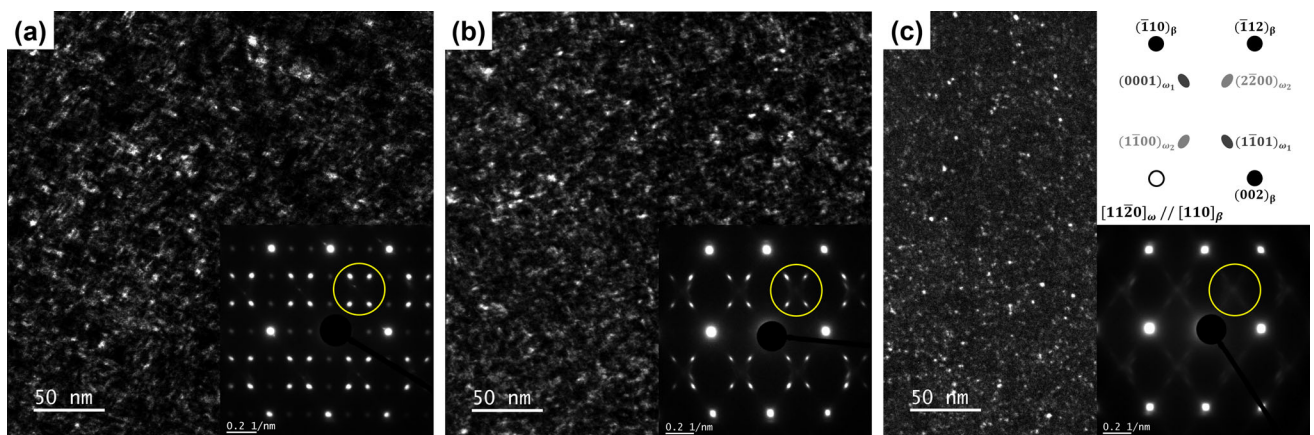

Fig. 3—The SAED patterns acquired along the $[110]_\beta$ zone axis with the corresponding DF/TEM micrographs selecting the ω-phase reflections (marked with the yellow circles) for Ti–14Nb (*a*), Ti–20Nb (*b*) and Ti–26Nb (*c*) alloys (Color figure online).

via the diffusion mechanism.[31] In this case, the phase appeared after quenching from the β-phase field, confirming its identity as the athermal ω-phase. Reflections corresponding to the ω-phase were observed in all analyzed materials; however, their intensity decreased with increasing concentrations of Nb (Figures 3(a) through (c)). This indicates that the amount of this phase decreases with the concentration of Nb. It is widely accepted that the content of the ω-phase decreases with the increasing stability of the β-phase[32] (or β-stabilizer concentration) and is suppressed in highly stabilized β-Ti alloys, such as Ti–18Mo.[33] The phase typically appears in the form of nanometric precipitates uniformly distributed within the β-matrix, which is also evident in this case, as seen in DF/TEM micrographs presented in Figures 3(a) through (c). Importantly, in addition to the content, the size of the precipitates also decreases with the increasing concentration of Nb in the analyzed materials.

Figure 4 shows a series of SAED patterns acquired along the $[113]_\beta$ zone axis. The presented patterns contain the ω-phase reflections (marked with the blue circles), along with the O′-phase reflections present at 1/

2 $\{112\}_\beta$ (marked with the red circle). The O′-phase exhibits orthorhombic symmetry (Cmcm) and can form from the β-phase by $\{011\}//<0\bar{1}1>_\beta$ shuffle, as previously reported, among others, in References 34 and 35. The occurrence of the O′-phase was reported in various oxygen-rich β-Ti alloys, such as Ti–23Nb–2O[35,36] or Ti2448 (gum metal).[34] The phase is present in the form of nanometric particles randomly distributed within the β-matrix, as seen in the DF/TEM image in Figure 4(b). The obtained SAED patterns show relatively intense reflections for the Ti–14Nb alloy, which then weaken for the Ti–20Nb and Ti–26Nb. This is most likely related to the increasing stability of the β-phase, which has a suppressing effect on O′ formation. However, a slightly higher concentration of oxygen (Table I) in Ti–14Nb may promote the formation of the phase.[37]

B. Mechanical Properties

The mechanical properties of the investigated alloys were studied with the application of both tensile and compression tests. Figure 5 presents the representative
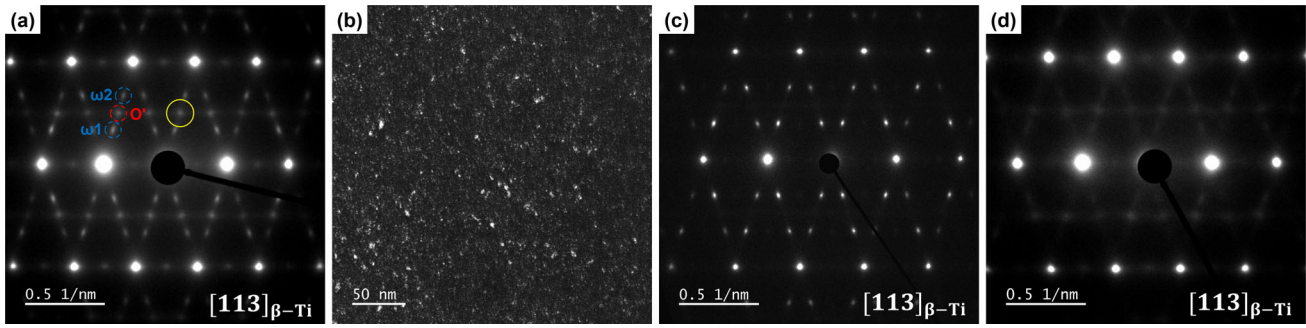
Fig. 4—The SAED patterns acquired along the [113]$_\beta$ zone axis for Ti–14Nb (a), along with the corresponding DF image (b), Ti–20Nb (c) and Ti–26Nb (d). The presented DF image selecting the O′-phase reflection (marked with the yellow circle) (Color figure online).
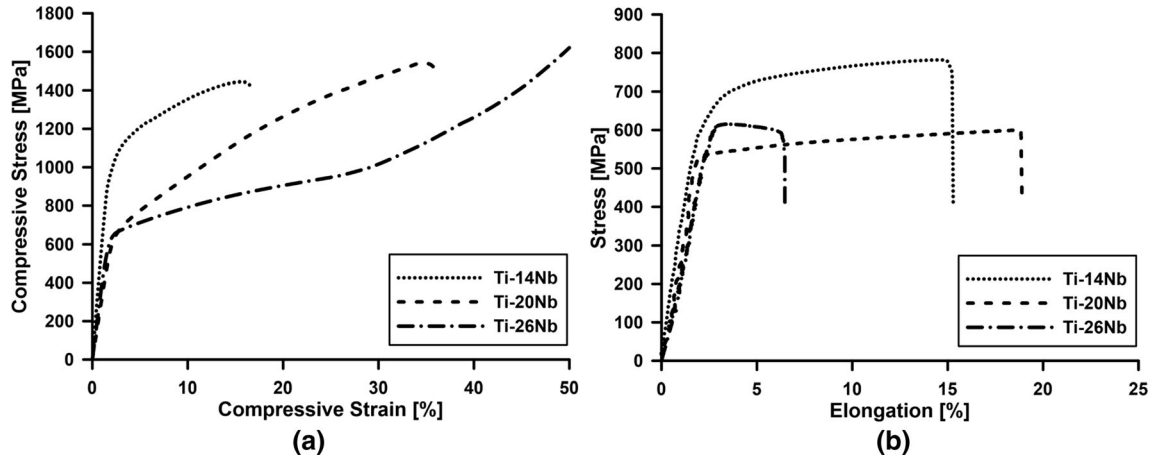

Fig. 5—Compression (a) and tension (b) stress–strain curves for the studied alloys.

Table II. Mechanical Properties of the Investigated Alloys—Yield Strength (YS) Measured in Compression (C) and Tension (T) Mode, Ultimate Tensile Strength (UTS) and Elongation

Alloy	YS (C) (MPa)	YS (T) (MPa)	UTS (MPa)	Elongation (Pct)
Ti–14Nb	860 ± 10	640 ± 20	770 ± 10	12 ± 3
Ti–20Nb	580 ± 40	540 ± 30	600 ± 30	15 ± 4
Ti–26Nb	630 ± 20	600 ± 20	620 ± 20	6 ± 2

stress-strain curves measured for the analyzed alloys, whereas Table II summarizes the obtained results. It is clearly visible that the highest YS (860 MPa in compression and 640 MPa in tension) was registered for Ti–14Nb. Subsequently, as the content of Nb increased to 20 at. pct, the yield strength decreased (580 MPa in compression and 540 MPa in tension), but then increased again in the case of Ti–26Nb (630 MPa in compression and 600 MPa in tension).

It is important to note that the yield strength values obtained from tensile and compression tests for Ti–20Nb and Ti–26Nb alloys are similar, with more significant differences observed only for Ti–14Nb. Similar effects were noted in previous studies; for instance, Gao et al.[38] reported an asymmetry in the yield strength values obtained from tensile and compression tests for the metastable β-phase Ti–7Mo–3Nb–3Cr–3Al

(wt pct) alloy (549 and 680 MPa, respectively), revealing a SIMT mechanism also found in the Ti–14Nb alloy (described in detail in Section III–D). This asymmetry is most likely associated with tension-compression asymmetry, a phenomenon widely studied in superelastic NiTi alloys resulting from the different stress-induced martensite variant selection during tension/compression.[39] Nevertheless, the general trend of yield strength changes in compression and tension modes remains consistent.

The fabricated materials showing relatively good plasticity, particularly in the compression mode—the lowest compressive strain of 18 pct was registered for Ti–14Nb, while no cracks were observed up to 50 pct for Ti–26Nb alloy (Figure 5(a)). On the other hand, ductility in the tensile mode was significantly reduced, as indicated by Figure 5(b). Figure 6 displays a series of

SEM images depicting the fracture morphology of the samples after the tensile test. It is clearly visible that the fractures primarily exhibit a brittle mode, with cracks propagating mainly along the grain boundaries. This is most probably related to the occurrence of TiC carbides located at the grain boundaries, as illustrated in Figures 1(b) and (c). However, there is also evidence of ductile behavior in the investigated materials, manifested by the occurrence of fine dimples, as shown in the inserts in Figures 6(a) through (c).

C. Superelastic Properties

Cyclic compressive tests were used to determine the superelasticity of the manufactured alloys. The analysis was conducted at RT by incrementally increasing the strain by 0.5 pct, from 1.0 to 5.0 pct, as shown in Figure 7. To measure the recoverable strain the value of permanent strain that occurred after the last cycle was subtracted from the maximum strain, in this case 5 pct. The results of this measurements are summarized in
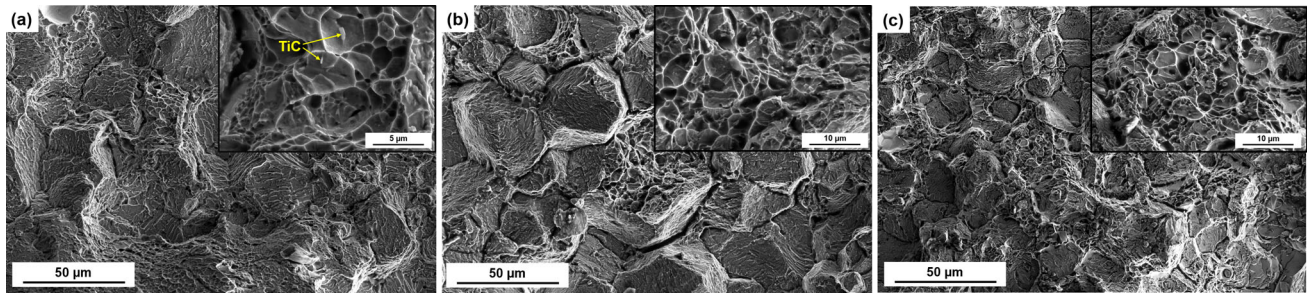

Fig. 6—SEM images of fracture morphology after the tensile test of Ti–14Nb (a), Ti–20Nb (b) and Ti–26Nb (c).
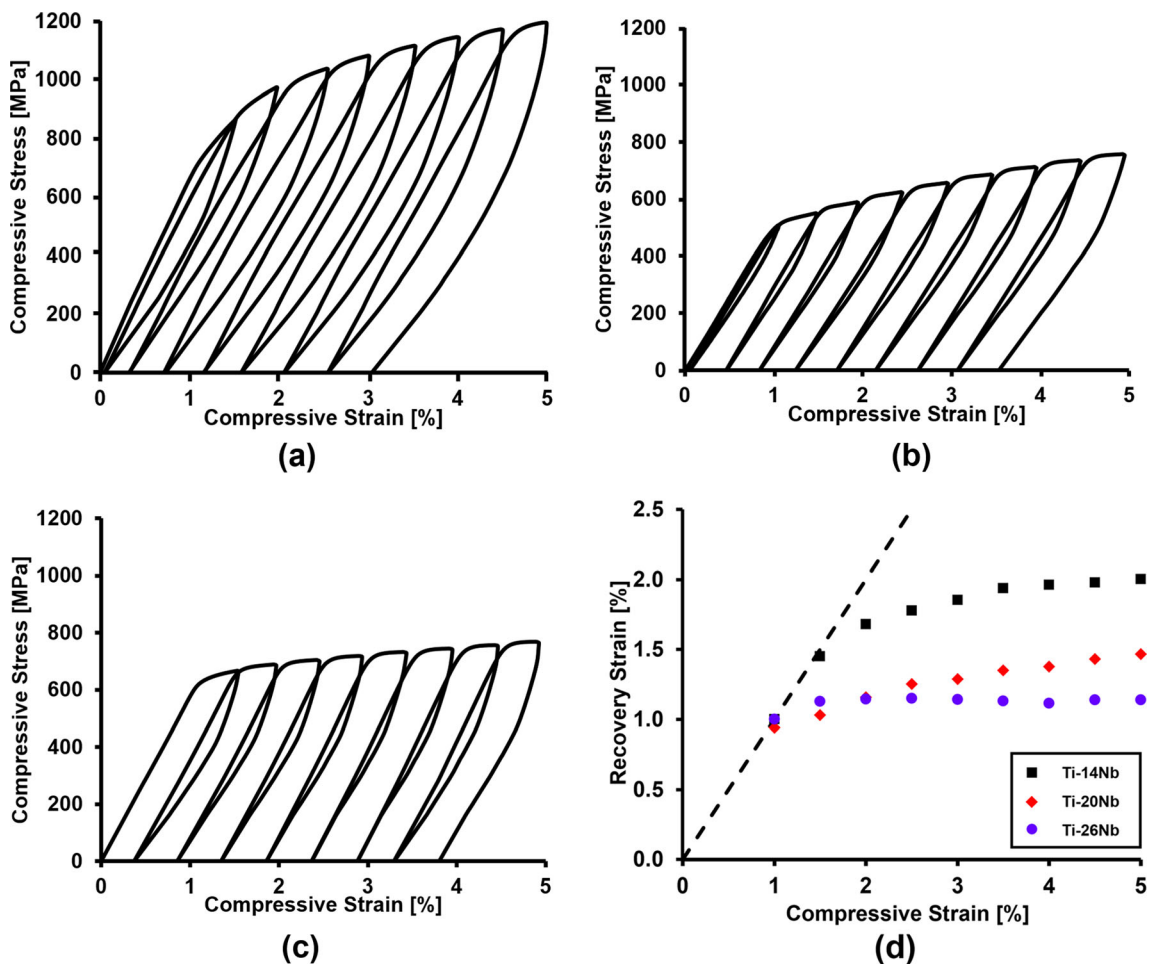

Fig. 7—Cyclic compression stress–strain curves of Ti–14Nb (a), Ti–20Nb (b), Ti–26Nb (c) alloys and recovered strain as a function of compressive strain (d).

Table III. The highest recoverability of 2.0 pct was recorded for Ti–14Nb. With the increasing concentration of Nb, the value of recoverable strain decreases to 1.4 pct for Ti–20Nb and next to 1.1 pct for the Ti–26Nb. One can see that for Ti–20Nb and Ti–26Nb alloys the strain is recoverable only in the first cycle (1.0 pct), which is associated with elastic deformation. In the following cycles, permanent deformation occurs, as resulted from Figure 7(d). This shows that the SIMT mechanism is not active during the loading of these materials. For Ti–14Nb, the strain is fully recoverable up to the second cycle (1.5 pct) and nearly recoverable in the third cycle (2.0 pct). This indicates that the alloy exhibits the superelastic response as a result of the reversible SMIT mechanism.

Figure 8 shows the values of depth recovery ratio (η_h) and work recovery ratio (η_w) of the investigated alloys in relation to an indentation depth, calculated as described in the experimental section (Eqs. [1] and [2]). The presented data points represent the mean value derived from a minimum of 10 indentations. At the constant indentation depth, the strain recovery significantly increases with the decreased concentration of Nb, e.g., at the depth of 100 nm the work recovery ratio increases from about 35 pct for Ti–26Nb to 60 pct for Ti–14Nb. This tendency next persists with the increasing indentation depth up to the end of the analyzed range. This observation is consistent with the macroscopic behavior of the materials investigated by the cyclic compressions tests (Figure 7) since it was found that their recoverable strain decreased with the increasing Nb content. On the other hand, the compression tests indicate near perfect strain recoverability of Ti–14Nb alloy up to 2 pct. In the case of the nanoindentation test the values of both η_h

and η_w deviate from 100 pct even at the lowest force of 5 mN corresponding to indentation depth of about 80 nm. This is most probably associated with the different stress distribution generated in the materials by these methods. Although the uniaxial compression test produces a relatively simple and homogenous stress field distributed throughout the entire volume of the sample, the stresses formed during nanoindentation are rather complex and highly localized. The studies show that the stresses generated by the indenter during nanoindentation decrease radially with the distance from the tip.[24] This resulted in the occurrence of multiple zones in which different processes occur, i.e., plastically deformed martensite zone located directly under the tip, encompassed by a reversible martensite area, incompletely transformed zone and non-transformed β-phase zone.[24,40] Thus, once the stress under the tip exceeds the critical stress for dislocation slip, it initiates permanent deformation, leading to diminished recoverability.[40] The presence of the plastically deformed zone beneath the tip even at low indentation depth is a reason for the reduced recoverability that was observed also in other works, e.g., References 24 and 25. Zhou et al.[25] showed that the magnitude of the strain recovery is closely related to the type of the indenter tip. In this case, almost no recovery was observed for the Berkovich tip exhibited high representative strain. However, for the spherical tips, the recoverability increases with the radius of the indenter and reaches near 100 pct for the tip radius of 200 μm, which was mainly associated with the elastic response.[25] In this work, we used a spherical indenter with a smaller radius of 5 μm exhibiting higher representative strain to activate the SIMT during the loading and to reduce the permanent deformation in comparison to the Berkovich tip. Although the SIMT can take place only in the limited area of the strained zone beneath the indent, it is visible that the strain recoverability significantly decreases with the increasing Nb concentration in the investigated materials. This means that with the increasing Nb concentration, the SIMT mechanism disappears,

Table III. Recoverable Strains for the Ti–xNb Alloys Calculated Based on Cyclic Compression Stress–Strain Curves

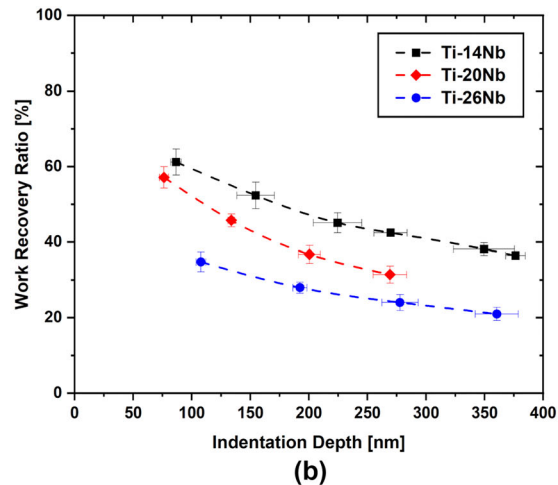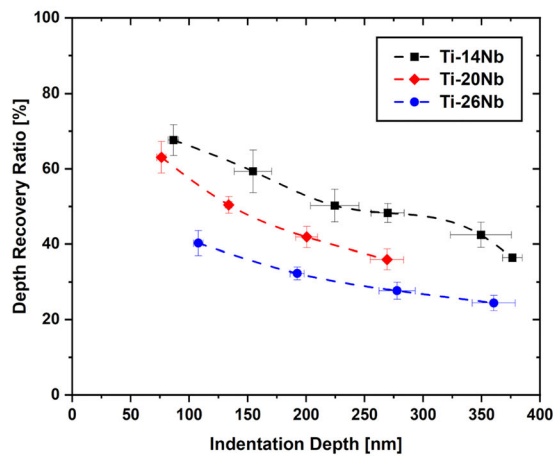| Alloy	Ti–14Nb	Ti–20Nb	Ti–26Nb
Recoverable Strain (Pct)	2.0 ± 0.1	1.4 ± 0.2	1.1 ± 0.1

Fig. 8—Depth recovery ratio (a) and work recovery ratio (b) with respect to indentation depth for the investigated materials.

whereas residual strain recoverability is connected with the elastic response.

D. Deformation Behavior

Figure 9 presents the optical microscopy (OM) images of the series of Ti–xNb alloys acquired within the in situ loading tests. The microstructure of the alloys was studied in the following sequence: (i) initial state, (ii) loaded state (ε = 2 pct in tensile), and (iii) after unloading. The obtained results revealed that the deformation characteristics of those alloys exhibit a distinct dissimilarity. It is clearly visible, that for Ti–14Nb the deformation led to the development of fine needles within the grains, which subsequently vanished upon stress removal. This observation suggests that the initial phase of its deformation is governed by the SIMT mechanism. This is consistent with the data acquired from cyclic compressive tests, as the alloy demonstrated the occurrence of the superelastic phenomenon. With the increasing Nb content to 20 at. pct the deformation mechanism evolved to a twinning—the twin structure formed during the deformation remains unchanged after the unloading. In contrast, there were no signs of any reversible transformations or twin

formation observed for the Ti–26Nb alloy, leading to the conclusion that its deformation proceeds via the slip mechanism. In order to confirm those observations the EBSD technique was applied.

Figure 10 presents an EBSD orientation map of the deformed Ti–20Nb. One may notice, the presence of several micrometer-thick twinning bands within the β-grains. The performed analysis of the misorientation distribution along the line crossing two of such bands (Figures 10(b) and (c)), indicates that they exhibited a misorientations angle of about 50 deg with respect to the matrix. This is a characteristic misorientation angle for {332}<113> twinning system. The other bands have also been identified as {332} <113> twins and marked on the orientation maps with black lines. On the other hand, Figure 11(a) presents the map acquired for a sample of deformed Ti–26Nb alloy. In this case, no twins were observed. Instead of that, noticeable misorientations in the grains of the β-phase may be registered. Figure 11(b) shows the kernel average misorientation (KAM) map, which may be applied for the qualitative representation of the density of dislocations in the materials.[41] The KAM values were categorized into color-coded ranges, with blue indicating the lowest KAM values (0 to 1 deg) and red the highest values (4 to
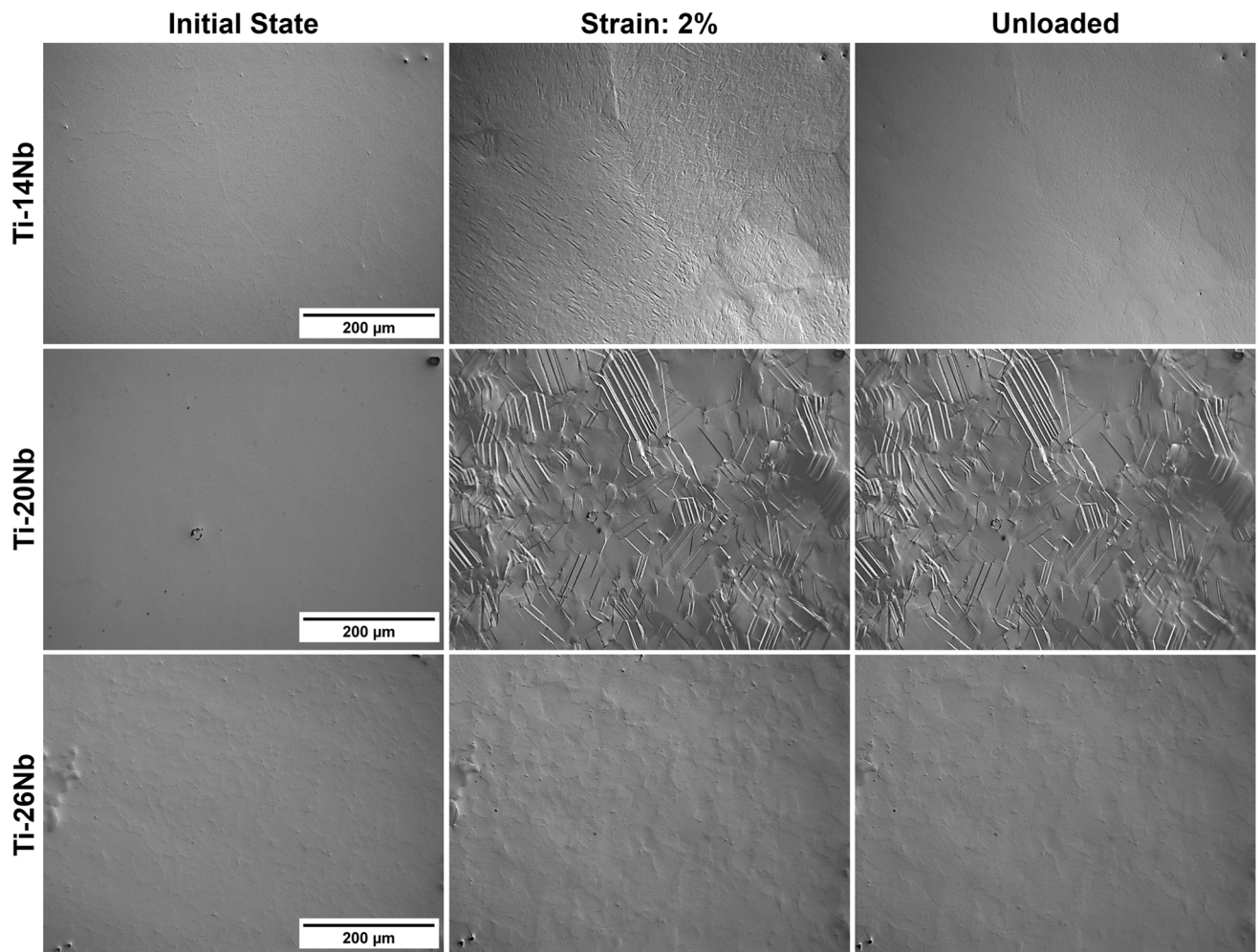

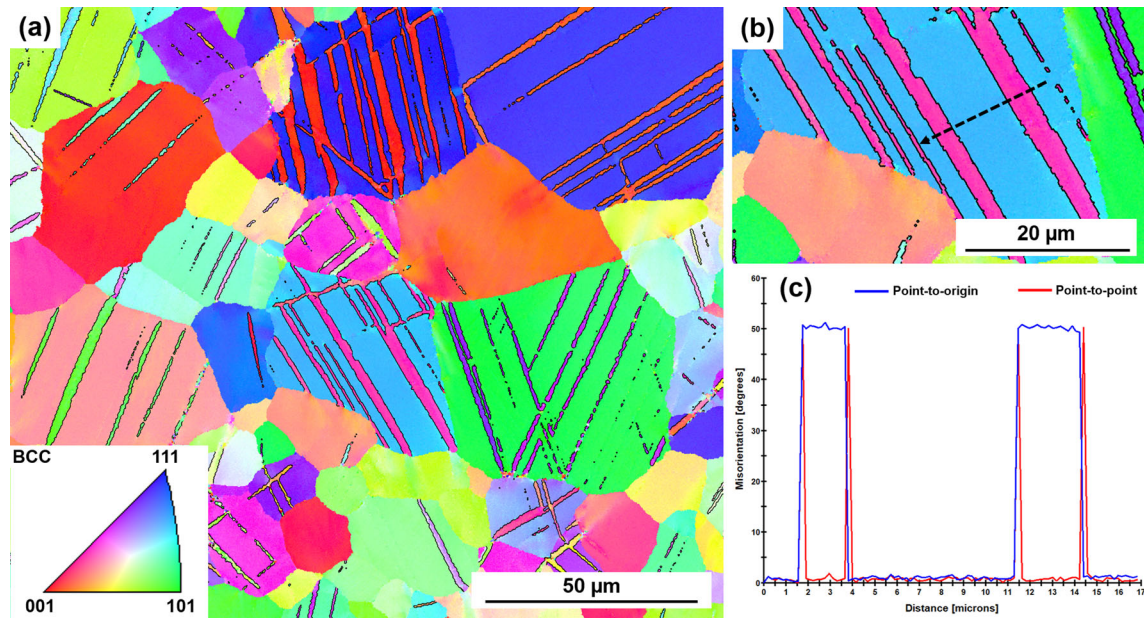Fig. 9—The microstructures of the Ti–xNb acquired during the *in situ* tensile experiment.

Fig. 10—EBSD orientation map of the deformed Ti–20Nb alloy (*a*), magnified area (*b*) with the corresponding misorientation profile (*c*). The {332}<113> twin boundaries were marked by the black lines.
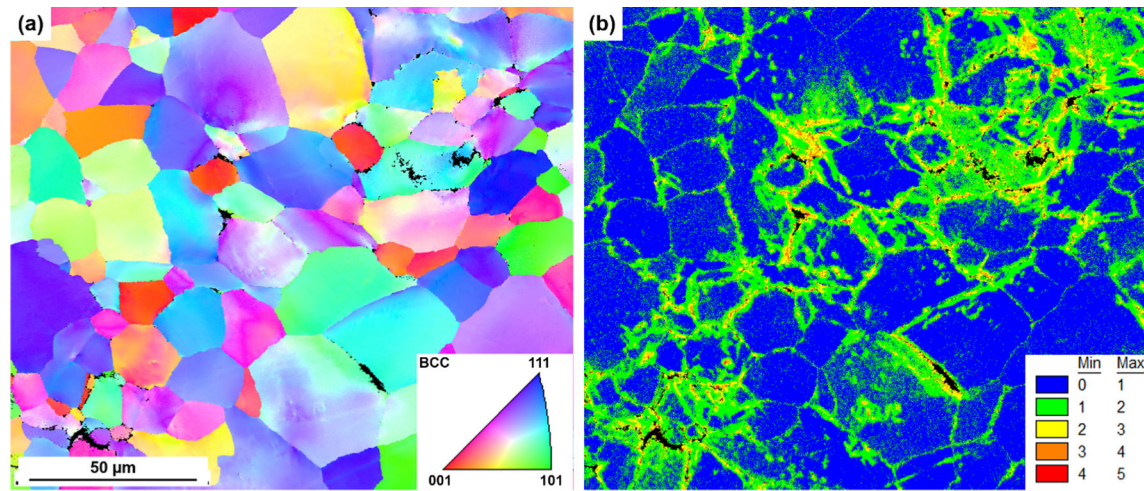

Fig. 11—EBSD orientation map of the deformed Ti–26Nb alloy (*a*) and the corresponding KAM map (*b*).

5 deg). The misorientations higher than 5 deg were excluded from the calculations. The obtained results indicate increased values of KAM in the vicinity of grain boundaries, suggesting that dislocations are primarily concentrated in those regions. This confirms the previous conclusion concerning the occurrence of dislocation slip as a main deformation mechanism for the Ti-26Nb alloy.

IV.   DISCUSSION

A. *Microstructure*

The microstructural analysis of the fabricated alloys indicates that they comprised the relatively fine β-Ti grains and precipitates of TiC carbide located primarily at the grain boundaries. Similar microstructures were previously registered for various β-Ti alloys prepared using the PM, *e.g.*, Ti–17Nb–8Zr.[42] However, the application of the mixture of elemental powders during the sintering typically resulted in the occurrence of much larger grains[21,43]; for example, Ti–22Nb sintered using the SPS from the blend of Ti and Nb powders exhibited large grains, with the size exceeding 200 μm.[20] This shows a favorable impact of the mechanical alloying on the grain refinement in the sintered β-Ti alloys. However, one of the main drawbacks concerning the preparation of the materials using the PM is the elevated concentration of interstitial contaminations in comparison to materials fabricating using the casting

technology.[44] In this case, the raised carbon content led to the development of TiC precipitates (Figure 1). Carbon exhibits extremely low solubility in titanium. According to ASTM Standard Specifications, to prevent the formation of carbides in CP-Ti, the carbon concentration must be maintained below 0.08 wt pct (0.3 at. pct for pure Ti).[45] This serves as the carbon limit in the variety of $\alpha + \beta$- and β-Ti alloys. This is also in accordance with the predication of the pseudobinary Ti–Nb–C phase diagram by Thermo-Calc software.[45] On the other hand, the TiC carbides were observed in the sintered Ti–Nb-based alloys containing even lower contents of carbon, such as 0.05 wt pct (0.2 at. pct).[30] Similarly, in the presented work, the presence of TiC carbides were observed in all fabricated materials, despite the overall carbon content (as shown in Table I) being significantly lower than the specified limit value. The following two contamination pathways are typically observed in materials synthesized using the MA—process control agent (PCA) and wear of MA vessel/balls.[46] Taking into consideration, the reports concerning the extensive dissolution of carbon and hydrogen in the milled Ti powders in the presence of organic compounds e.g., in Reference 47, the synthesis was performed without any PCA. This leads to the conclusion that the main source of contamination was the wear process of the MA vessel/balls, in this case, made of cemented tungsten carbide. The WC particles that have been introduced to the powder during the milling most probably dissolved in the matrix during the sintering/solution treatment and next precipitated as TiC carbides during cooling, since the solubility of C in β-phase decreases with the temperature.[28]

Oxygen is another common impurity in Ti alloys fabricated using the PM techniques.[48] The increased concentrations of oxygen were typically present in the β-Ti alloys fabricated using the PM as an effect of the high chemical affinity of oxygen to Ti. In the investigated Ti–xNb alloys the concentration of this element reaches 0.5 to 0.6 at. pct (measured using the IGF method). However, considering the available data, this value is one of the lowest reported for alloys prepared using the mechanical alloying, since the typical oxygen concentrations in these materials reached 1 to 4 at. pct.[20,42,43] In contrast to carbon, oxygen exhibited high solubility in Ti—up to 8 at. pct in the β-Ti phase.[49] Taking into consideration the relatively low oxygen content in the investigated materials, it may be concluded that it is present in the solid solution. This confirms also the microstructural observation since no phases enriched in the oxygen were found in all analyzed alloys.

B. Mechanical Properties

Considering the mechanical properties of the prepared Ti–Nb alloys (Table II), the Ti–14Nb exhibited the highest yield strength of 860 MPa in compression (C) and 640 MPa in tension (T). As the content of Nb increases to 20 at. pct, this value drops down to 580 MPa (C) and 540 MPa (T), and roses again for Ti-26Nb alloy to 630 MPa (C) and 600 MPa (T). The yield strengths measured for the investigated materials significantly exceed the values described for their conventionally fabricated counterparts. For instance, yield strength of Ti–26Nb, which is the most frequently investigated composition, typically ranges from 200 to 350 MPa after the solution treatment[11,50] and reaches up to 500 MPa in the aged state.[14,51] It is worth noting that the YS of the materials used for bone implants are typically higher than those exhibited by the conventional Ti–Nb alloys. The values of 300–550 MPa are observed for CP-Ti alloys, 800 to 1000 MPa for Ti–6Al–4V, $\approx$ 900 MPa for Ti–6Al–7Nb, and 500 to 1500 MPa for Co–Cr–Mo alloys.[52] Improved strength of the investigated materials can be attributed to the synergistic impact of solid solution strengthening by Nb and O, as well as the presence of titanium carbides. Kim et al.[53] reported, that oxygen highly increases the strength of the β-Ti alloys. They observed an remarkable increase in the yield strength of solution-treated Ti–22Nb from about 400 MPa to above 1000 MPa by introducing 2 at. pct of O. Similarly, the presence of carbide precipitates in titanium alloys has been found to enhance their strength, e.g., Sarkar et al.[54] reported that the addition of 0.2 wt pct (0.8 at. pct) of C to the cast Ti-15-3 β-titanium alloy resulted in an increase in yield strength from 1026 to 1216 MPa, attributed to a presence of TiC precipitates. In this case, the carbon content was significantly lower (0.16 to 0.08 at. pct), resulting in a reduced strengthening effect caused by the presence of TiC. The carbides were primarily located at the grain boundaries (Figure 1), leading to limited ductility of the fabricated materials during tensile tests. This was associated with the brittle behavior of TiC, which provided suitable sites for the nucleation and propagation of cracks.[55] Furthermore, their presence acted as stress concentrators, localizing plastic deformation near the grain boundaries. This effect is particularly noticeable in the Ti–26Nb alloy, where the plastic deformation was almost entirely restricted to the zone close to the grain boundaries (Figure 11). However, a similar effect likely occurs for Ti-14 as well as Ti–20Nb, leading to the nucleation of martensite/twins close to the carbides located at the grain boundaries. In contrast to the cast Ti–Nb alloys, these fabricated by the PM route generally exhibited high yield strengths of above 1000 MPa, as reported in several studies.[18,19,47] Such high values of YS resulted from the elevated contents of oxygen typically presented in the sintered titanium alloys.[18,19] For example, Lai et al.[18] reported the values varied from about 800 to 1300 MPa for a series of pressureless sintered Ti–xNb alloys containing of about 0.7 wt pct of oxygen. Even higher YS of about 1500 MPa was reported for the Ti alloy containing 11 at. pct of Nb and 4 at. pct of oxygen.[19] On the other hand, the elevated YS of these materials were commonly combined with the poor ductility or even brittleness.[19,56] The experimental conditions proposed within this work resulted in a decrease of the oxygen concentration to 0.6

at. pct, which ensure improved ductility of the prepared alloys.

The observed changes in YS could be understood as a result of the cooperation of several factors, including: grain size strengthening (I), solid solution strengthening by Nb (II), and interstitial contaminations (III), the occurrence of ω-phase precipitates (IV), and finally, the critical resolved shear stress (CRSS) of the SIMT/twinning/slip mechanisms (V). As shown in Table I, the Ti–14Nb alloy exhibited the largest grain size of 47 μm, correlating with the highest yield strength. Considering this, it appears that grain size may not be a key factor influencing the mechanical properties of the investigated materials. Similarly, these variations cannot be simply attributed to the solid solution strengthening effect caused by the substitutional Nb atoms. It is well-known that interstitial contaminations can significantly affect the mechanical properties of β-Ti alloys. However, in this case, the contents of O, N, and H (Table I) in all alloys were at similar levels. Therefore, they shouldn't have an essential impact on their YS values. More notable differences were observed only for carbon: 0.16, 0.10, and 0.08 at. pct for Ti–14Nb, Ti–20Nb, and Ti–26Nb, respectively. However, in this case, carbon should have a limited effect on the YS values, as it contributed to the formation of TiC carbides located at the grain boundaries (Figure 1). Recent studies suggest that the occurrence of nanometric precipitates of the ω-phase in the parent β-phase may significantly affect the observed YS of materials. For instance, Lai et al.[57] reported a significant increase in the YS of Ti–25Nb–0.7Ta–2Zr alloy (from 350 to 490 MPa) as a result of changes in deformation behavior caused by the presence of fine ω-phase particles. As depicted in Figure 3, ω-phase precipitates were also found in this work. However, their occurrence alone cannot explain the increase in the YS value between Ti–20Nb and Ti–26Nb. TEM analysis revealed that the content of the ω-phase decreases with the concentration of Nb (as described also in other works, e.g., Reference 32). This suggests that the CRSS had the most significant effect on the observed changes in YS for the studied materials. While recent research indicates that the CRSS for SIMT is expected to be lower than that for $\{332\}\langle113\rangle_\beta$ twinning,[58] it is conceivable that, in this specific scenario, the elevated oxygen level increases this value to the extent that it surpasses that of twinning, ultimately leading to a decrease in YS for the Ti–20Nb alloy. This observation may be supported by the fact that the SIMT in β-Ti alloys containing elevated levels of interstitial oxygen may be suppressed due to lattice distortions generated by the oxygen atoms occupying octahedral sites.[59] On the other hand, slip becomes more favorable in highly stabilized β-Ti alloys, as observed in various systems, including Ti–V, Ti–Mo, or Ti–Nb.[60,61] The transition from $\{332\}\langle113\rangle_\beta$ twinning to slip typically results in increased strength accompanied by limited ductility, as also observed in this work for the Ti–26Nb alloy.

Recent studies have revealed that the deformation behavior of β-Ti alloys is closely related to the stability of the parent phase, which can be quantitatively described with respect to the chemical composition using a Mo equivalence (Mo_{eq}) value.[62] In general, with the increasing concentration of the β-stabilizing elements (or Mo_{eq}), the following mechanisms are activated: α''-martensite deformation, stress-induced martensitic transformation, twinning and slip.[60,63] Therefore, to understand the origin of nonlinear changes in YS, the early stages of the deformation of the investigated materials were studied in more detail (Section III–D).

The SIMT occurred for the sintered Ti–14Nb (Mo_{eq} = 6.7) alloy. However, it was previously registered for alloys containing more than 26 at. pct of Nb (Mo_{eq} = 11.3)[64] or for ternary ones with similar Mo_{eq}, e.g., Ti–22Nb–5Ta (Mo_{eq} = 11.7),[65] Ti–22Nb–1Mo (Mo_{eq} = 11.5)[66] or more complex Ti–7.5Nb–4Mo–1Sn (Mo_{eq} = 10.9).[67] The presence of this specific deformation mechanism in Ti–14Nb was confirmed by both microstructural as well as mechanical analysis. The performed in situ tensile experiments (Figure 9) provided direct evidence of martensite formation within the microstructure of the alloy during the loading, which subsequently disappeared upon the removal of stress. This is also in agreement with the cyclic tests, since the material exhibit superelastic properties. Those observations are especially important since the occurrence of the SIMT mechanisms in oxygen-added β-Ti alloys was questioned in the literature, e.g., Tahara et al.[68,69] stated that presence of oxygen (1 at. pct) in Ti-(23, 26)Nb suppresses the martensitic transformation and that the superelastic effect arose from the reversible growth of oxygen-rich nanodomains.

With the increasing stability of the β-phase, the critical stress for SIMT (σSIMT) increases and the twinning becomes more favorable.[63] The mechanism was previously observed e.g., in Ti–5Mo–2W (Mo_{eq} = 11.4),[70] Ti–6.5Mo (Mo_{eq} = 12),[71] Ti–24V (Mo_{eq} = 13.4)[72] or Ti–8Mo (Mo_{eq} = 15).[73] In the case of the Ti–Nb system, twinning was found in materials with Nb concentration exceeding approximately 27 at. pct (Mo_{eq} = 11.7).[74] On the other hand, in the presented work the mechanism was detected for the Ti–20Nb (Mo_{eq} = 9.1). One can see that this alloy exhibited the lowest YS (580 $\pm$ 40 MPa) among the investigated materials. The works show that the Ti–Nb-based alloys that exhibit the twinning mechanism typically possess a low yield strengths below 500 MPa, enhanced work-hardening rate and excellent deformability.[71] Such alloys are referred to as the new group of β-Ti alloys displaying the twinning-induced plasticity (TWIP) effect.[75] The $\{112\}\langle111\rangle$ twinning mode was identified as the dominant mode in metals with a BCC structure, including Fe, Nb, Mo, and their alloys.[76] However, the less common $\{332\}\langle113\rangle$ system was observed in some β-Ti alloys.[74,77] In this work also the $\{332\}\langle113\rangle$ mode was registered to be active during the loading of the sintered Ti–20Nb. Recent studies have shown that the

transformation pathway in β-Ti alloys exhibiting the TWIP effect can be highly intricate.[78,79] Qian et al.[79] demonstrated that a specific deformation mechanism in the β-phase Ti–12Mo alloy may be closely related to the crystallographic orientation of the grain. In this case, the selection of the dominant mechanism is connected to the value of the Schmid factor for the activation of SIMT/twinning, along with the accompanying transformation strain associated with a specific martensite variant. This results in three possible deformation modes, including: (I) {332}<113>$_β$ twinning, (II) SIMT, and (III) a combination of both mechanisms, resulting in {332}<113>$_β$ twinning assisted by martensite {130}<310>$_{α''}$ twinning. A similar effect was observed in other works, such as,[58] where the deformation mechanism of the Ti–12Mo alloy was tuned from SIMT to a combination of SIMT and {332}<113>$_β$ twinning, and finally, single {332}<113>$_β$ twinning by progressively increasing Zr content from 3 to 10 at. pct.

Increased contents of the β-stabilizing elements lead to a shift in the deformation mechanism towards slip.[60] This mechanism is prevalent in the heavily stabilized β-alloys, such as Ti–5Mo–2.5Fe (Mo_{eq} = 16.0)[80] or Ti–8Mo–1Fe (Mo_{eq} = 17.5).[81] It was found that for the binary Ti–Nb alloys, the Nb concentration required to activate this mechanism varied from 32 to 36 at. pct (Mo_{eq} = 13.4 to 14.6).[60] Typically, they demonstrate elevated strength accompanied by a reduced work-hardening rate.[81] As with the previous cases, for the investigated materials this mechanism was observed at a lower Mo_{eq} value—in Ti–26Nb alloy (Mo_{eq} = 11.4). The transition of the predominating mechanism to slip resulted in the increase of the value of the YS from 580 ± 40 MPa (Ti–20Nb) to 630 ± 20 MPa (Ti–26Nb). A similar effect was reported in other works, for example the transition from twinning to slip as a result of addition 1 at. pct of Fe to Ti–8Mo resulted in the enhancement of the yield strength of this alloy from 440 to 840 MPa.[81]

The above considerations indicate that the specific deformation mechanisms occur at the reduced content of the β-stabilizing elements compared with the alloys prepared by the conventional technologies. Because the presence of deformation mechanisms is intimately linked to the stability of the parent β-phase, there has to be another factor, except the β-stabilizers concentration, that increases its stability. The recent results show that although oxygen is typically considered to be an α-stabilizer, it can simultaneously affect the β-phase stability. Oxygen by occupying the octahedral sites suppresses the martensitic transformation.[59] This is associated with the counter effect between the strain fields around this sites and $(0\bar{1}1)[011]$ shuffling mode needed for the formation of martensite.[59] This leads to the decrease of the α''-martensite stability, which in turn results in the significant drop of the M_s that was also reported in other works.[11,18] In our case, the stabilizing effect of oxygen on the β-phase resulted in the occurrence not only of the SIMT mechanism at lower Nb concentration but also of other mechanisms—twinning and slip.

C. Superelastic Properties

The occurrence of the superelastic effect in the conventionally manufactured metastable β-Ti alloys is well-established.[14,82] Numerous works show that the best properties are observed for alloys containing about 26 at. pct of Nb (or similar Mo_{eq}).[11,14,82] It also has been revealed that the materials with the same compositions, but fabricated by powder metallurgy or additive manufacturing, do not exhibit superelasticity.[20,83,84] This is also true for the present work—the data acquired during the cyclic compression tests for the sintered Ti–26Nb alloy (Figure 7(c)) indicate only permanent deformation. A similar effect was observed for Ti–20Nb, however, considering the recovery strain vs. the compressive strain curve (Figure 7(d)), a slight increase in the recovery strain may be observed in the following cycles, which may have resulted from the contribution of the SIMT mechanism. For those alloys, the recoverable strain reached 1.4 pct (Ti–20Nb) and 1.1 pct (Ti–26Nb). It is worth emphasizing that the total recoverable strain (R_T) measured in the cyclic compression tests contain three different terms associated with the various recovery mechanisms: elasticity (R_{EL}), pore structure (R_{POR}) and SIMT mechanism (R_{SIMT})[18]:

$$R_T = R_{EL} + R_{POR} + R_{SIMT}.$$

In the case of the investigated materials the R_{POR} term might be ignored since they were nearly fully dense (porosity below 0.1 vol pct). Considering the deformation characteristic of both Ti–26Nb and Ti–20Nb, it may be concluded that the observed R_T is predominantly associated with the R_{EL} term. On the other hand, different behavior was observed for Ti–14Nb alloy, since it exhibited the stress-strain hysteresis in loading-unloading cycles associated with the reversible SIMT mechanism (Figure 7(a)). The obtained value of R_T for this material reached 2.0 pct. This value is comparable with the values previously reported for the conventionally fabricated Ti–Nb alloys after the solution treatment, varied from 1.6 to 2.5 pct.[11,13,14] Higher values up to 4.2 pct were observed for the aged Ti–26Nb alloy.[11] However, those alloys possess relatively low $σ_{SIMT}$ in the range of 100 to 200 MPa and a YS of 300 to 400 MPa when compared with the investigated materials. Extremely high values of recoverable strain were reported for a few sintered Ti–Nb-based alloys, for instance Lai et al.[18] showed 5.0 pct of recoverable strain for the Ti–13Nb. Similarly, Yuan et al.[19] reported a value of 5.4 pct for the sintered Ti–11Nb–4O alloy. However, those alloys did not possess the typical stress–strain hysteresis for the superelastic materials; the high values of the recoverable strains resulted rather from the occurrence of very high YS and enhanced elasticity, than from the reversible SIMT mechanism, e.g., the

mentioned Ti–13Nb showed an elevated YS of $\approx$ 1200 MPa but low elastic modulus of 25 GPa (measured by the compression tests).[18] Although the β-Ti alloys are characterized by high elasticity, the Ti–Nb alloys possess elastic modules varying between 50 and 80 GPa.[82] Taking this into consideration, these results may be slightly affected by the measurement error. Nevertheless, the observations presented in the frame of this work indicate that it is possible to fabricate Ti–Nb alloys that exhibit the superelastic phenomenon at RT by use of the PM. However, to make it possible the content of Nb needs to be decreased from the initial 26 at. pct to about 14 at. pct. This is attributed to the higher content of the interstitial contaminations in comparison to the cast alloys, which significantly decreases the martensitic transformation temperature.

Nevertheless, the superelastic response of the discussed Ti–14Nb differs in comparison to that which is observed for conventional β-Ti or NiTi alloys. Typically, two distinct yielding points can be distinguished on the stress-strain curves for superelastic alloys: the initial point corresponds to the activation of the SIMT mechanism, while the latter to permanent deformation.[23] Surprisingly, one yielding point was observed on stress–strain curves of the studied Ti–14Nb (Figure 7(c)), although they demonstrate the superelastic properties. The same effect was registered for various β-Ti alloys characterized by the elevated content of interstitial contaminations.[53,85] While this phenomenon remains not fully understood, its origins may be linked to the presence of interstitial oxygen atoms within the structure of these alloys. The first-principle calculations by Salloom et al.[59] indicate the presence of the significant lattice distortions in the β-phase around the octahedral sites occupied by oxygen. The locally induced stain fields, generated by randomly distributed O atoms, leads to the formation of nanoscale $\{110\}<1\bar{1}0>$ traverse lattice modulations that may disturb long-range order during the SIMT.[68] These modulations are similar to the recently reported O′-phase, which was found in various oxygen-rich β-Ti alloys.[34,35,86] The O′-phase was also found in the investigated alloys (Figure O). The superelastic effect in β-Ti alloys arises from the reversible $\beta \rightarrow \alpha''$ martensitic transformation, proceeding through a $\{112\}<111>$ shear (lattice distortion) followed by a $\{110\}<1\bar{1}0>$ shuffle (lattice modulation).[87] However, the randomly distributed O′-particles/traverse lattice modulations may impede the $\{112\}<111>$ shear required for the SIMT, thereby inhibiting the long-range martensitic transformation.[34,68,88] This phenomenon was experimentally observed for the $\beta \rightarrow \alpha'$ transformation in low-stabilized Ti–4Al–4Fe–0.25Si–0.1O alloy. In this case, the shearing of O′-nanodomains during the deformation disrupts the primary martensite transformation, leading to the initiation of a secondary martensite transformation.[87] The suppressing impact of the O′-particles on the SIMT may significantly increase the critical stress for the transformation. In a specific case, this value can become similar to the critical stress for the slip deformation, resulting in a one-stage yielding behavior. A similar hypothesis was proposed by Castany et al.[89] to describe the one-stage yielding phenomena in superelastic Ti–24Nb–0.5O. Through in situ synchrotron X-ray diffraction studies, they found that the suppressing effect of oxygen on the martensitic transformation led to an increase in the critical stress required for the transformation, approaching values similar to the critical stress for twinning/slip deformation. This observation aligns with the results obtained in the nanoindentation experiment (Figure 8), as perfect recoverability was not observed even at relatively low stress levels. This suggests the cooperation of SIMT and plastic deformation during the indentation. The presence of the ω-phase has also been considered a significant obstacle to the martensitic transformation.[11] However, in this case, its presence cannot explain the phenomenon of the one-yielding effect. This is because the occurrence of the ω-phase has been previously reported in various β-Ti superelastic alloys that exhibit the standard two-yielding behavior, as seen in Ti–26Nb.[11] Nevertheless, to observe this phenomenon of SIMT in interstitials-rich β-Ti alloys the concentration of the β-stabilizing elements has to be reduced taking into consideration their effect on the β-phase stability. The findings of this study are expected to serve as a basic for the development of new superelastic metastable β-Ti alloys, particularly those produced with the application of the newly developed powder metallurgy and additive manufacturing technologies.

V. CONCLUSIONS

1. The proposed fabrication technology involved the preparation of the pre-alloyed powders by mechanical alloying and their consolidation by hot pressing is an attractive approach for the fabrication of Ti–Nb-based alloys with enhanced mechanical properties in comparison to materials produced using conventional technologies.
2. The deformation characteristic of β-Ti alloys is closely related to the concentration of the β-stabilizers. As concentration of β-stabilizing elements increases, the following deformation mechanisms were registered: SIMT $(\beta \rightarrow \alpha'') \rightarrow$ twinning $\rightarrow$ slip. Each of these mechanisms was observed at a reduced content of Nb compared to analogous alloys obtained using conventional techniques, which is most probably associated with the elevated concentration of oxygen that may affect the stability of the parent β-phase. The evolution of the deformation mechanisms was responsible for the nonlinear changes in YS with the Nb concentration. It was found that the substantial reduction of YS of the fabricated Ti–20Nb was related to the transition of the predominant deformation mechanism from SIMT to $\{332\}<113>$ twinning. The next increase in the value of YS for the sintered Ti–26Nb was accompanied by a shift in the deformation mode to slip

3. The superelasticity in the sintered β-Ti alloys, may be achieved by the reduction of concentration of β-stabilizing elements compared to the alloys manufactured with the application of the conventional casting techniques, which is most probably related to the occurrence of the interstitials. In the presented work, the best superelasticity, with the 2.0 pct of the recoverable strain, were registered for the Ti–14Nb, whereas for conventionally fabricated Ti–Nb alloys superelasticity occurs at Nb concentration of about 26 at. pct. The developed material demonstrates non-conventional, one-stage yielding behavior, resulting in the occurrence of superelastic response at significantly higher stresses (close to YS, in this case, 860 MPa) when compared with the its conventionally manufactured counterparts, for which the effect is observed typically below 300 to 400 MPa.

ACKNOWLEDGMENTS

CONFLICT OF INTEREST

On behalf of all authors, the corresponding author states that there is no conflict of interest.

OPEN ACCESS

REFERENCES

1. S.S. Sidhu, H. Singh, and M.A.H. Gepreel: *Mater. Sci. Eng. C*, 2021, vol. 121, p. 111661 https://doi.org/10.1016/J.MSEC.2020.111661.
2. L.C. Zhang and L.Y. Chen: *Adv. Eng. Mater.*, 2019, vol. 21(4), p. 1801215. https://doi.org/10.1002/ADEM.201801215.
3. A. Biesiekierski, J. Wang, M. Abdel-Hady Gepreel, and C. Wen: *Acta Biomater.*, 2012, vol. 8(5), pp. 1661–69. https://doi.org/10.1016/j.actbio.2012.01.018.
4. A. Sotniczuk, D. Kuczyńska-Zemła, P. Kwaśniak, M. Thomas, and H. Garbacz: *Electrochim. Acta*, 2019, vol. 312, pp. 369–79. https://doi.org/10.1016/J.ELECTACTA.2019.04.138.
5. Q. Chen and G.A. Thouas: *Mater. Sci. Eng. R*, 2015, vol. 87, pp. 1–57. https://doi.org/10.1016/J.MSER.2014.10.001.
6. Y. Al-Zain, H.Y. Kim, H. Hosoda, T.H. Nam, and S. Miyazaki: *Acta Mater.*, 2010, vol. 58(12), pp. 4212–23. https://doi.org/10.1016/j.actamat.2010.04.013.
7. D. Kalita, Ł Rogal, T. Czeppe, A. Wójcik, A. Kolano-Burian, P. Zackiewicz, B. Kania, and J. Dutkiewicz: *J. Mater. Eng. Perform.*, 2020, vol. 29(3), pp. 1445–52. https://doi.org/10.1007/s11665-019-04417-0.
8. J.I. Kim, H.Y. Kim, T. Inamura, H. Hosoda, and S. Miyazaki: *Mater. Sci. Eng. A*, 2005, vol. 403(1–2), pp. 334–39. https://doi.org/10.1016/j.msea.2005.05.050.
9. A. Ramezannejad, W. Xu, W.L. Xiao, K. Fox, D. Liang, and M. Qian: *Curr. Opin. Solid State Mater. Sci.*, 2019, vol. 23(6), p. 100783. https://doi.org/10.1016/J.COSSMS.2019.100783.
10. H.Y. Kim, N. Oshika, J.I. Kim, T. Inamura, H. Hosoda, and S. Miyazaki: *Mater. Trans.*, 2007, vol. 48(3), pp. 400–06. https://doi.org/10.2320/matertrans.48.400.
11. H.Y. Kim, Y. Ikehara, J.I. Kim, H. Hosoda, and S. Miyazaki: *Acta Mater.*, 2006, vol. 54(9), pp. 2419–29. https://doi.org/10.1016/j.actamat.2006.01.019.
12. H.Y. Kim, Y. Ohmatsu, J. Kim, H. Hosoda, and S. Miyazaki: *Mater. Trans.*, 2004, vol. 45(4), pp. 1090–95. https://doi.org/10.2320/matertrans.45.1090.
13. J. Zhang, F. Sun, Y. Hao, N. Gozdecki, E. Lebrun, P. Vermaut, R. Portier, T. Gloriant, P. Laheurte, and F. Prima: *Mater. Sci. Eng. A*, 2013, vol. 563, pp. 78–85. https://doi.org/10.1016/j.msea.2012.11.045.
14. H.Y. Kim, H. Satoru, J.I. Kim, H. Hosoda, and S. Miyazaki: *Mater. Trans.*, 2004, vol. 45(7), pp. 2443–48. https://doi.org/10.2320/matertrans.45.2443.
15. Z.Z. Fang, J.D. Paramore, P. Sun, K.S.R. Chandran, Y. Zhang, Y. Xia, F. Cao, M. Koopman, and M. Free: *Int. Mater. Rev.*, 2018, vol. 63(7), pp. 407–59. https://doi.org/10.1080/09506608.2017.1366003.
16. T. Zhang and C.T. Liu: *Adv. Powder Mater.*, 2022, vol. 1(1), p. 100014. https://doi.org/10.1016/j.apmate.2021.11.001.
17. Y. Chen, P. Han, A. Dehghan-Manshadi, D. Kent, S. Ehtemam-Haghighi, C. Jowers, M. Bermingham, T. Li, J. Cooper-White, and M.S. Dargusch: *J. Mech. Behav. Biomed. Mater.*, 2020, vol. 104, p. 103691 https://doi.org/10.1016/j.jmbbm.2020.103691.
18. M. Lai, Y. Gao, B. Yuan, and M. Zhu: *Mater. Des.Des.*, 2015, vol. 87, pp. 466–72. https://doi.org/10.1016/j.matdes.2015.07.180.
19. B. Yuan, B. Yang, Y. Gao, M. Lai, X.H. Chen, and M. Zhu: *Mater. Des.Des.*, 2016, vol. 92, pp. 978–82. https://doi.org/10.1016/j.matdes.2015.12.148.
20. A. Terayama, N. Fuyama, Y. Yamashita, I. Ishizaki, and H. Kyogoku: *J. Alloys Compd.*, 2013, vol. 577, pp. S408-12. https://doi.org/10.1016/j.jallcom.2011.12.166.
21. N. Sakaguchi, M. Niinomi, T. Akahori, J. Takeda, and H. Toda: *Mater. Sci. Eng. CC*, 2005, vol. 25(3), pp. 370–76. https://doi.org/10.1016/j.msec.2005.04.003.
22. N. Sakaguchi, M. Niinomi, T. Akahori, J. Takeda, and H. Toda: *Mater. Sci. Eng. CC*, 2005, vol. 25(3), pp. 363–69. https://doi.org/10.1016/j.msec.2004.12.014.
23. S.M.K. Yamauchi, I. Ohkata, and K. Tsuchiya: *Shape Memory and Superelastic Alloys Applications and Technologies*, Woodhead Publishing in Materials, Oxford, 2011, pp. 3–41.
24. Y. Zhou, A. Fillon, D. Laillé, and T. Gloriant: *Mater Charact*, 2022, vol. 184, p. 111691 https://doi.org/10.1016/J.MATCHAR.2021.111691.

25. Y. Zhou, A. Fillon, H. Jabir, D. Laillé, and T. Gloriant: *Surf. Coat. Technol.*, 2021, vol. 405, p. 126690 https://doi.org/10.1016/J.SURFCOAT.2020.126690.
26. H. Tsuda, T. Ozaki, and S. Mori: *Mater. Trans.*, 2020, vol. 61(6), pp. 1090–95. https://doi.org/10.2320/matertrans.MT-M2019318.
27. Z.Q. Chen, Y.G. Li, D. Hu, M.H. Loretto, and X. Wu: *Mater. Sci. Technol.*, 2003, vol. 19(10), pp. 1391–98. https://doi.org/10.1179/026708303225005999.
28. M. Yan, M. Qian, C. Kong, and M.S. Dargusch: *Acta Biomater.*, 2014, vol. 10(2), pp. 1014–23. https://doi.org/10.1016/j.actbio.2013.10.034.
29. P. Wanjara, R.A.L. Drew, J. Root, and S. Yue: *Acta Mater.*, 2000, vol. 48(7), pp. 1443–50. https://doi.org/10.1016/S1359-6454(99)00453-X.
30. D. Zhao, K. Chang, T. Ebel, M. Qian, R. Willumeit, M. Yan, and F. Pyczak: *J. Mech. Behav. Biomed. Mater.*, 2013, vol. 28, pp. 171–82. https://doi.org/10.1016/j.jmbbm.2013.08.013.
31. M. Li and X. Min: *Sci. Rep.*, 2020, vol. 10(1), pp. 1–15. https://doi.org/10.1038/s41598-020-65254-z.
32. S. Hanada and O. Izumi: *Metall. Trans. A*, 1987, vol. 18(2), pp. 265–71. https://doi.org/10.1007/BF02825707.
33. X. Zhao, M. Niinomi, M. Nakai, and J. Hieda: *Acta Biomater.*, 2012, vol. 8(5), pp. 1990–97. https://doi.org/10.1016/j.actbio.2012.02.004.
34. Q. Liang, Y. Zheng, D. Wang, Y. Hao, R. Yang, Y. Wang, and H.L. Fraser: *Scripta Mater.*, 2019, vol. 158, pp. 95–99. https://doi.org/10.1016/j.scriptamat.2018.08.043.
35. T. Li, M. Lai, A. Kostka, S. Salomon, S. Zhang, C. Somsen, M.S. Dargusch, and D. Kent: *Scripta Mater.*, 2019, vol. 170, pp. 183–88. https://doi.org/10.1016/j.scriptamat.2019.06.008.
36. D. Kalita, Ł Rogal, P. Bobrowski, T. Durejko, T. Czujko, A. Antołak-Dudka, E. Cesari, and J. Dutkiewicz: *Materials*, 2020, vol. 13(12), pp. 1–14. https://doi.org/10.3390/ma13122827.
37. L.S. Wei, H.Y. Kim, and S. Miyazaki: *Acta Mater.*, 2015, vol. 100, pp. 313–22. https://doi.org/10.1016/j.actamat.2015.08.054.
38. P. Gao, J. Fan, F. Sun, J. Cheng, L. Li, B. Tang, H. Kou, and J. Li: *J. Alloys Compd.*, 2019, https://doi.org/10.1016/j.jallcom.2019.151762.
39. X. Chen, W. Chen, Y. Ma, Y. Zhao, C. Deng, X. Peng, and T. Fu: *Mech. Mater.*, 2020, vol. 145, p. 103402 https://doi.org/10.1016/j.mechmat.2020.103402.
40. G.A. Shaw, D.S. Stone, A.D. Johnson, A.B. Ellis, and C. Crone: *Appl. Phys. Lett.*, 2003, vol. 83, pp. 257–59. https://doi.org/10.1063/1.1591235.
41. M.N. Gussev and K.J. Leonard: *J. Nucl. Mater.*, 2019, vol. 517, pp. 45–56. https://doi.org/10.1016/J.JNUCMAT.2019.01.034.
42. M.W.D. Mendes, C.G. Ágreda, A.H.A. Bressiani, and J.C. Bressiani: *Mater. Sci. Eng. C*, 2016, vol. 63, pp. 671–77. https://doi.org/10.1016/j.msec.2016.03.052.
43. D.R. dos Santos, V.A. Rodrigues Henriques, C.A. Alves Cairo, and M. dos Santos Pereira: *Mater. Res.*, 2005, vol. 8(4), pp. 439–42. https://doi.org/10.1590/s1516-14392005000400014.
44. A. Amherd Hidalgo, R. Frykholm, T. Ebel, and F. Pyczak: *Adv. Eng. Mater.*, 2017, vol. 19(6), pp. 1–14. https://doi.org/10.1002/adem.201600743.
45. D. Zhao, T. Ebel, M. Yan, and M. Qian: *Jom*, 2015, vol. 67(10), pp. 2236–43. https://doi.org/10.1007/s11837-015-1590-6.
46. C. Suryanarayana: *Prog. Mater. Sci.*, 2001, vol. 46(1–2), pp. 1–184. https://doi.org/10.1016/S0079-6425(99)00010-9.
47. J. Keskinen, A. Pogany, J. Rubin, and P. Ruuskanen: *Mater. Sci. Eng. A*, 1995, vol. 196(1–2), pp. 205–11. https://doi.org/10.1016/0921-5093(94)09701-1.
48. E. Baril, L.P. Lefebvre, and Y. Thomas: *Powder Metall.*, 2013, vol. 54(3), pp. 183–87. https://doi.org/10.1179/174329011X13045076771759.
49. M. Cancarevic, M. Zinkevich, and F. Aldinger: *Calphad*, 2007, vol. 31(3), pp. 330–42. https://doi.org/10.1016/J.CALPHAD.2007.01.009.
50. Y. Fukui, T. Inamura, H. Hosoda, K. Wakashima, and S. Miyazaki: *Mater. Trans.*, 2004, vol. 45(4), pp. 1077–82. https://doi.org/10.2320/matertrans.45.1077.
51. L.L. Chang, Y.D. Wang, and Y. Ren: *Mater. Sci. Eng. A*, 2016, vol. 651, pp. 442–48. https://doi.org/10.1016/j.msea.2015.11.005.
52. K. Prasad, O. Bazaka, M. Chua, M. Rochford, L. Fedrick, J. Spoor, R. Symes, M. Tieppo, C. Collins, A. Cao, D. Markwell, K. Ostrikov, and K. Bazaka: *Materials*, 2017, vol. 10(8), p. 884. https://doi.org/10.3390/MA10080884.
53. J.I. Kim, H.Y. Kim, H. Hosoda, and S. Miyazaki: *Mater. Trans.*, 2005, vol. 46(4), pp. 852–57. https://doi.org/10.2320/matertrans.46.852.
54. R. Sarkar, P. Ghosal, T.K. Nandy, and K.K. Ray: *Philos. Mag.*, 2013, vol. 93(15), pp. 1936–57. https://doi.org/10.1080/14786435.2013.765979.
55. T. Ali, L. Wang, X. Cheng, D. Gu, Z. Zhou, and X. Min: *Mater. Des.*, 2022, vol. 214, p. 110395 https://doi.org/10.1016/j.matdes.2022.110395.
56. M. Wen, C. Wen, P. Hodgson, and Y. Li: *Mater. Des.*, 2014, vol. 56, pp. 629–34. https://doi.org/10.1016/j.matdes.2013.11.066.
57. M.J. Lai, T. Li, and D. Raabe: *Acta Mater.*, 2018, vol. 151, pp. 67–77. https://doi.org/10.1016/j.actamat.2018.03.053.
58. B. Qian, J. Zhang, Y. Fu, F. Sun, Y. Wu, J. Cheng, P. Vermaut, and F. Prima: *J. Mater. Sci. Technol.*, 2021, vol. 65, pp. 228–37. https://doi.org/10.1016/j.jmst.2020.04.078.
59. R. Salloom, D. Reith, R. Banerjee, and S.G. Srinivasan: *J. Mater. Sci.*, 2018, vol. 53(16), pp. 11473–87. https://doi.org/10.1007/s10853-018-2381-6.
60. R.P. Kolli, W.J. Joost, and S. Ankem: *JOM*, 2015, vol. 67(6), pp. 1273–80. https://doi.org/10.1007/s11837-015-1411-y.
61. S. Hanada, T. Yoshio, and O. Izumi: *Trans. Jpn Inst. Met.*, 1986, vol. 27(7), pp. 496–503. https://doi.org/10.2320/matertrans1960.27.496.
62. R. Boyer, G. Welsch, and E.W. Collings: *Materials Properties Handbook: Titanium Alloys*, ASM International, Materials Park, 1994, pp. 3–12.
63. M. Abdel-Hady, K. Hinoshita, and M. Morinaga: *Scripta Mater.*, 2006, vol. 55(5), pp. 477–80. https://doi.org/10.1016/j.scriptamat.2006.04.022.
64. M. Tahara, H.Y. Kim, H. Hosoda, and S. Miyazaki: *Acta Mater.*, 2009, vol. 57(8), pp. 2461–69. https://doi.org/10.1016/j.actamat.2009.01.037.
65. H.Y. Kim, S. Hashimoto, J.I. Kim, T. Inamura, H. Hosoda, and S. Miyazaki: *Mater. Sci. Eng. A*, 2006, vol. 417(1–2), pp. 120–28. https://doi.org/10.1016/j.msea.2005.10.065.
66. D.C. Zhang, Y.F. Mao, Y.L. Li, J.J. Li, M. Yuan, and J.G. Lin: *Mater. Sci. Eng. A*, 2013, vol. 559, pp. 706–10. https://doi.org/10.1016/j.msea.2012.09.012.
67. D.C. Zhang, J.G. Lin, W.J. Jiang, M. Ma, and Z.G. Peng: *Mater. Des.*, 2011, vol. 32(8–9), pp. 4614–17. https://doi.org/10.1016/j.matdes.2011.03.024.
68. M. Tahara, H.Y. Kim, T. Inamura, H. Hosoda, and S. Miyazaki: *Acta Mater.*, 2011, vol. 59(16), pp. 6208–18. https://doi.org/10.1016/j.actamat.2011.06.015.
69. M. Tahara, H.Y. Kim, T. Inamura, H. Hosoda, and S. Miyazaki: *J. Alloys Compd.*, 2013, vol. 577, pp. S404-07. https://doi.org/10.1016/j.jallcom.2011.12.113.
70. F. Sun, J.Y. Zhang, M. Marteleur, C. Brozek, E.F. Rauch, M. Veron, P. Vermaut, P.J. Jacques, and F. Prima: *Scripta Mater.*, 2015, vol. 94, pp. 17–20. https://doi.org/10.1016/J.SCRIPTAMAT.2014.09.005.
71. F. Sun, J.Y. Zhang, M. Marteleur, T. Gloriant, P. Vermaut, D. Laillé, P. Castany, C. Curfs, P.J. Jacques, and F. Prima: *Acta Mater.*, 2013, vol. 61(17), pp. 6406–17. https://doi.org/10.1016/j.actamat.2013.07.019.
72. X.L. Wang, L. Li, W. Mei, W.L. Wang, and J. Sun: *Mater Charact.*, 2015, vol. 107, pp. 149–55. https://doi.org/10.1016/j.matchar.2015.06.038.
73. X. Min, X. Chen, S. Emura, and K. Tsuchiya: *Scripta Mater.*, 2013, vol. 69(5), pp. 393–96. https://doi.org/10.1016/J.SCRIPTAMAT.2013.05.027.
74. P. Castany, Y. Yang, E. Bertrand, and T. Gloriant: *Phys. Rev. Lett.*, 2016, vol. 117(24), pp. 1–6. https://doi.org/10.1103/PhysRevLett.117.245501.
75. L. Lilensten, Y. Danard, R. Poulain, R. Guillou, J.M. Joubert, L. Perrière, P. Vermaut, D. Thiaudière, and F. Prima: *Materialia*, 2020, vol. 12, p. 100700 https://doi.org/10.1016/J.MTLA.2020.100700.
76. J.W. Christian and S. Mahajan: *Prog. Mater. Sci.*, 1995, vol. 39(1–2), pp. 1–157. https://doi.org/10.1016/0079-6425(94)00007-7.
77. S. Shin, C. Zhu, and K.S. Vecchio: *Mater. Sci. Eng. A*, 2018, vol. 724, pp. 189–98. https://doi.org/10.1016/j.msea.2018.03.062.

78. B. Qian, M. Yang, L. Lilensten, P. Vermaut, F. Sun, and F. Prima: *Mater. Res. Lett.*, 2022, vol. 10(2), pp. 45–51. https://doi.org/10.1080/21663831.2021.2013967.
79. B. Qian, L. Lilensten, J. Zhang, M. Yang, F. Sun, P. Vermaut, and F. Prima: *Mater. Sci. Eng. A*, 2021, vol. 822, p. 141672 https://doi.org/10.1016/j.msea.2021.141672.
80. X. Min, S. Emura, F. Meng, G. Mi, and K. Tsuchiya: *Scripta Mater.*, 2015, vol. 102, pp. 79–82. https://doi.org/10.1016/J.SCRIPTAMAT.2015.02.018.
81. X.H. Min, S. Emura, N. Sekido, T. Nishimura, K. Tsuchiya, and K. Tsuzaki: *Mater. Sci. Eng. ASci. Eng. A*, 2010, vol. 527(10–11), pp. 2693–2701. https://doi.org/10.1016/J.MSEA.2009.12.050.
82. R.P. Kolli and A. Devaraj: *Metals*, 2018, vol. 8(7), pp. 1–41. https://doi.org/10.3390/met8070506.
83. L.C. Zhang, D. Klemm, J. Eckert, Y.L. Hao, and T.B. Sercombe: *Scripta Mater.*, 2011, vol. 65(1), pp. 21–24. https://doi.org/10.1016/j.scriptamat.2011.03.024.
84. M. Fischer, P. Laheurte, P. Acquier, D. Joguet, L. Peltier, T. Petithory, K. Anselme, and P. Mille: *Mater. Sci. Eng. CSci. Eng. C*, 2017, vol. 75, pp. 341–48. https://doi.org/10.1016/j.msec.2017.02.060.
85. M. Besse, P. Castany, and T. Gloriant: *Acta Mater.*, 2011, vol. 59(15), pp. 5982–88. https://doi.org/10.1016/j.actamat.2011.06.006.
86. Y. Zheng, R.E.A. Williams, S. Nag, R. Banerjee, H.L. Fraser, and D. Banerjee: *Scripta Mater.*, 2016, vol. 116, pp. 49–52. https://doi.org/10.1016/j.scriptamat.2016.01.024.
87. S. Lee, C. Park, J. Hong, and J.T. Yeom: *Sci. Rep.*, 2018, vol. 8(1), pp. 1–9. https://doi.org/10.1038/s41598-018-30059-8.
88. H.Y. Kim, L. Wei, S. Kobayashi, M. Tahara, and S. Miyazaki: *Acta Mater.*, 2013, vol. 61(13), pp. 4874–86. https://doi.org/10.1016/j.actamat.2013.04.060.
89. P. Castany, A. Ramarolahy, F. Prima, P. Laheurte, C. Curfs, and T. Gloriant: *Acta Mater.*, 2015, vol. 88, pp. 102–11. https://doi.org/10.1016/j.actamat.2015.01.014.